

# Off-axis afterglow light curves and images from 2D hydrodynamic simulations of double-sided GRB jets in a stratified external medium

Jonathan Granot,<sup>1,2\*</sup> Fabio De Colle<sup>3</sup> and Enrico Ramirez-Ruiz<sup>4,5</sup>

<sup>1</sup>Department of Natural Sciences, The Open University of Israel, P.O. Box 808, Ra'anana 43537, Israel

<sup>2</sup>Department of Physics, The George Washington University, Washington, DC 20052, USA

<sup>3</sup>Instituto de Ciencias Nucleares, Universidad Nacional Autónoma de México, A. P. 70-543 04510 D. F. Mexico

<sup>4</sup>TASC, Department of Astronomy & Astrophysics, University of California, Santa Cruz, CA 95064, USA

<sup>5</sup>Niels Bohr Institute, University of Copenhagen, Blegdamsvej 17, DK-2100 Copenhagen, Denmark

Accepted 2018 September 05. Received 2018 September 05; in original form 2018 March 15

## ABSTRACT

Gamma-ray burst (GRB) jets are narrow, and thus typically point away from us. They are initially ultra-relativistic, causing their prompt  $\gamma$ -ray and early afterglow emission to be beamed away from us. However, as the jet gradually decelerates its beaming cone widens and eventually reaches our line of sight and the afterglow emission may be detected. Such orphan afterglows were not clearly detected so far. Nevertheless, they should be detected in upcoming optical or radio surveys, and it would be challenging to clearly distinguish between them and other types of transients. Therefore, we perform detailed, realistic calculations of the expected afterglow emission from GRB jets viewed at different angles from the jet's symmetry axis. The dynamics are calculated using 2D relativistic hydrodynamics simulations of jets propagating into different power-law external density profiles,  $\rho_{\text{ext}} \propto R^{-k}$  for  $k = 0, 1, 1.5, 2$ , ranging from a uniform ISM-like medium ( $k = 0$ ) to a stratified steady stellar-wind like profile ( $k = 2$ ). We calculate radio, optical and X-ray lightcurves, and the evolution of the radio afterglow image size, shape and flux centroid. This may help identify misaligned relativistic jets, whether initially ultra-relativistic and producing a GRB for observers within their beam, or (possibly intrinsically more common) moderately relativistic, in either (i) nearby supernovae Ib/c (some of which are associated with long duration GRBs), or (ii) in binary neutron star mergers, which may produce short duration GRBs, and may also be detected in gravitational waves (e.g. GW 170817/GRB 170817A with a weak prompt  $\gamma$ -ray emission may harbor an off-axis jet).

**Key words:** gamma-ray burst: general — ISM: jets and outflows — hydrodynamics — methods: numerical — relativistic processes — gravitational waves

## 1 INTRODUCTION

It has been realized early on (Rhoads 1997) that the ultra-relativistic outflows that power GRBs are likely collimated into narrow jets, and therefore their prompt emission might be too dim to detect unless the jet is pointed towards us. However, during the afterglow phase the jet decelerates by sweeping up the external medium and its emission is beamed into an increasing solid angle, and may become visible for observers at larger viewing angles  $\theta_{\text{obs}}$  from the jet's symmetry axis. Such an “orphan afterglow” without a detected prompt  $\gamma$ -ray emission was not clearly detected yet and could potentially teach us a lot about the jet's angular structure and degree of collimation (e.g. Woods & Loeb 1999; Nakar, Piran & Granot, 2002; Totani & Panaitescu 2002; Levinson et al. 2002; Huang, Dai & Lu 2002; Nakar & Piran 2003; Rhoads 2003; Gal-Yam et al.

2006; Zou, Wu & Dai 2007; Rossi, Perna & Daigne 2008; van Eerten, Zhang & MacFadyen 2010b; Ghirlanda et al. 2014; Lamb, Tanaka & Kobayashi 2018).

For convenience, most works assume a uniform conical jet with sharp edges at a half-opening angle  $\theta_j$  with an initial value of  $\theta_0$ , often referred to as a “top hat jet”. For such an initial jet angular structure, once the jet's Lorentz factor  $\Gamma$  decreases below  $1/\theta_0$  it comes into lateral causal contact and could start to significantly expand sideways, though the actual rate of lateral spreading is rather involved (e.g. Rhoads 1999; Sari, Piran & Halpern 1999; Granot et al. 2001; Zhang & MacFadyen 2009; Wygoda, Waxman & Frail 2011; van Eerten & MacFadyen 2012b; Granot & Piran 2012). Moreover, around the same time the jet's edge becomes visible for an observer along its symmetry axis ( $\theta_{\text{obs}} = 0$ ). This leads to a steepening of the afterglow flux decay rate for such “on-axis” observers, known as a “jet break” (e.g. Rhoads 1997, 1999; Sari, Piran & Halpern 1999; Panaitescu & Mészáros 1999). For  $0 < \theta_{\text{obs}} < \theta_0$

\* E-mail: granot@openu.ac.il (JG)

different parts of the jet’s edge become visible at somewhat different times causing a smoother and somewhat later jet break (e.g. Granot et al. 2001; van Eerten, Zhang & MacFadyen 2010b; De Colle et al. 2012b; Ryan et al. 2015). For “off-axis” observers outside of the jet’s initial aperture,  $\theta_{\text{obs}} > \theta_0$  (or  $\Gamma_0(\theta_{\text{obs}} - \theta_0) \gtrsim$  a few, where  $\Gamma_0$  is the initial Lorentz factor), the prompt GRB emission is strongly suppressed due to relativistic beaming, and is likely to be missed.

However, such a sharp outer edge for the jet is not very physical, and it is much more natural to expect the initial energy per solid angle  $\epsilon_0 = dE_0/d\Omega$  (and possibly also  $\Gamma_0$ ) in the jet to drop more gradually and smoothly outside of some jet core angle,  $\theta_c$ . Various different jet angular structures have been considered in the literature (e.g. Mészáros, Rees & Wijers 1998; Rossi, Lazzati & Rees 2002; Zhang & Mészáros 2002; Kumar & Granot 2003; Granot 2007; Granot & Ramirez-Ruiz 2013), where the most popular are a “universal structured jet” where  $\epsilon_0(\theta > \theta_c) \propto \theta^{-2}$  and a Gaussian jet where  $\epsilon_0 \propto \exp(-\theta^2/2\theta_c^2)$ , which can reproduce “on-axis” afterglow lightcurves that are broadly similar to observations and to those from a top hat jet (some jet structures can be ruled out as they do not produce the observed “on-axis” afterglow lightcurves, e.g. Granot & Kumar 2003; Granot 2005). Because of the strong relativistic beaming during the prompt GRB emission (as  $\Gamma_0 \gtrsim 100$  is typically required by compactness arguments) and the early afterglow, even a small amount of energy in outflow propagating towards an off-axis observer at the outer wings of the jet could dominate the observed flux over the strongly suppressed contribution from the much more energetic core of the jet. However, as the faster and more energetic parts of the jet near its core gradually decelerate as the jet sweeps up the external medium, they gradually come into view as their beaming cone reaches the line of sight. If the jet’s core contains the bulk of its energy (e.g. for an initially top hat jet or a Gaussian jet viewed from  $\theta/\theta_c \gtrsim$  a few) and  $\epsilon_0$  rises steeply enough towards the jet’s core, then the flux for an off-axis observer initially rises until the beaming cone of the jet’s core reaches the line of sight, and only then does the emission from the jet’s core start to dominate the observed flux, which peaks around that time and starts to decay, approaching the lightcurve for an on-axis observer (e.g. Granot et al. 2002; Kumar & Granot 2003; Eichler & Granot 2006).

Here we use numerical simulations of an initial top hat jet (De Colle et al. 2012a,b). Nonetheless, even such an initially top hat jet develops an egg-shaped bow shock structure on the dynamical time due to its interaction with the external medium (e.g. Granot et al. 2001; Zhang & MacFadyen 2009). This makes it somewhat more realistic and interesting to compare with observations. At early times the afterglow flux for an “off-axis” observer is dominated by emission from the slower material at the sides of the jet, and it is relatively sensitive to the jet’s initial angular structure. However, once the beaming cone of the jet’s core reaches the line of sight near the peak in the lightcurve it starts dominating the observed flux, which in turn becomes rather insensitive to the jet’s initial angular structure outside of its core. Therefore, we expect that the results presented here should be broadly similar to those for other jet angular structures in which most of the jet’s energy is contained within its narrow core (see, e.g., De Colle, Kumar & Aguilera-Dena 2018; Gill & Granot 2018). Moreover, such detailed properties of the afterglow lightcurves and image may help to more clearly distinguish between orphan GRB afterglows and other types of transients in upcoming surveys, which may otherwise be very challenging.

The main novelty of this work in calculating the off-axis af-

terglow emission for different viewing angles  $\theta_{\text{obs}}$  is (i) considering different external density profiles, namely  $\rho_{\text{ext}} \propto R^{-k}$  for  $k = 0, 1, 1.5, 2$ , and (ii) calculating in addition to the off-axis afterglow lightcurves also the corresponding afterglow images, and in particular the flux centroid motion and the evolution the image size and shape, which may be more readily compared to observations when the image is marginally resolved. Such relatively realistic and detailed calculations may be very useful for identifying orphan GRB afterglows within the zoo of different transients expected in upcoming surveys (also in the optical, e.g. LSST).

In § 2 we present radio, optical and X-ray afterglow lightcurves for a wide range of viewing angles  $\theta_{\text{obs}}$  for a jet propagating into a power law external density  $\rho_{\text{ext}} \propto R^{-k}$  ranging from a uniform ISM-like medium ( $k = 0$ ) to a profile expected for a steady stellar wind ( $k = 2$ ). In § 3 we calculate the corresponding afterglow images in the radio and show the evolution of the image size, shape and flux centroid. There are two main motivations behind this. First, this may help identify misaligned relativistic jets in nearby supernovae Ib/c (Granot & Loeb 2003; Granot & Ramirez-Ruiz 2004; Soderberg, Frail & Wieringa 2004; Granot, Ramirez-Ruiz & Loeb 2005; Ramirez-Ruiz et al. 2005a; Bietenholtz et al. 2010, 2014; Xu, Nagataki & Huang 2011; Sobacchi et al. 2017) that are either (i) initially ultra-relativistic jets that produce a long GRB whose prompt  $\gamma$ -ray emission is strongly beamed away from us, or (ii) initially mildly relativistic jets, that may be more numerous. Second, in order to help infer the presence of a relativistic jet in compact binary mergers involving one or two neutron stars (NS-NS or NS-BH), and constrain our viewing angle and the jet’s angular structure (Rezzolla et al. 2011; Murguia-Berthier et al. 2014; Nagakura et al. 2014; Duffell, Quataert & MacFadyen 2015; Ruiz et al. 2016; Murguia-Berthier et al. 2017; Lazzati et al. 2017a,b; Lamb & Kobayashi 2017). This is naturally also motivated by the recent binary neutron star merger GW 170827/GRB 170817A that was detected in gravitational waves and had a weak prompt  $\gamma$ -ray emission and still shows a rising afterglow lightcurve from radio to X-rays (e.g. Abbott et al. 2017a,b,c; Goldstein et al. 2017; Haggard et al. 2017; Margutti et al. 2017; Hallinan et al. 2017; Drout et al. 2017; Lamb & Kobayashi 2018; Ruan et al. 2018; Margutti et al. 2018; Lyman et al. 2018; Mooley et al. 2018; Lazzati et al. 2018,?; Nakar & Piran 2018). In § 4 we discuss the scaling of our results with the model parameters, and how our results may help break degeneracies between the model parameters. Our conclusion are discussed in § 5

## 2 OFF-AXIS AFTERGLOW LIGHTCURVES FOR A JET IN A POWER-LAW EXTERNAL DENSITY PROFILE

For the calculations presented here we use 2D hydrodynamic simulations from De Colle et al. (2012b), based on the special relativistic hydrodynamics code *Mezcal*, and a complimentary code for calculating the radiation by post-processing the results of the numerical simulations De Colle et al. (2012a). The initial conditions for the GRB jet were a conical wedge of half-opening angle  $\theta_0 = 0.2$  rad, taken out of the spherical self-similar Blandford & McKee (1976) solution. The simulation starts when the Lorentz factor of the material just behind the shock is  $\Gamma = 20$ . The calculation of the synchrotron radiation is supplemented by adding the contribution from a Blandford & McKee (1976) conical wedge at earlier times, corresponding to  $20 \leq \Gamma \leq 500$  (which causes an artificially sharp transition in the light curve between the two at a rather early time). The simulation was for an isotropic equivalent kinetic energy of

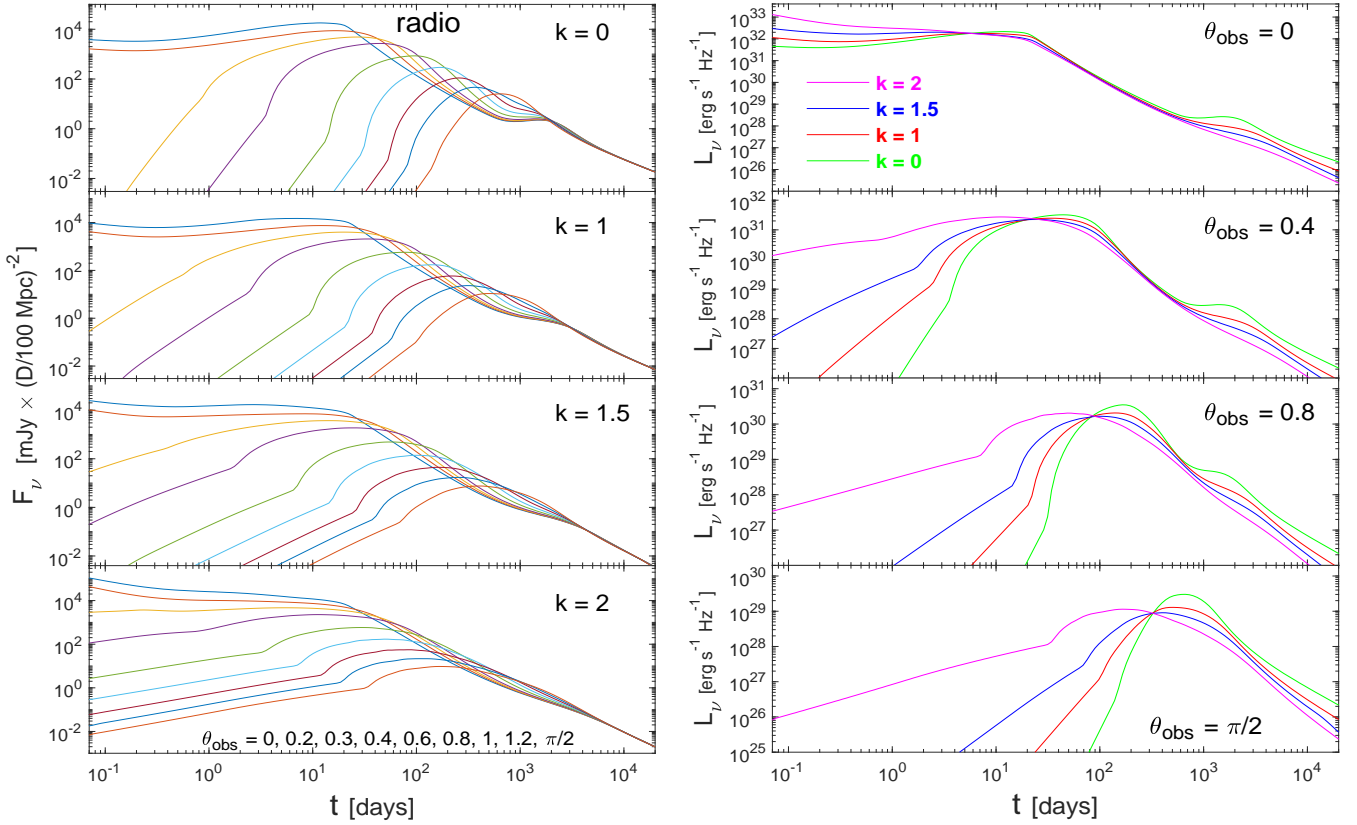


**Figure 1.** Radio light curves ( $\nu = 8.46$  GHz) for hydrodynamic simulations of an initially conical jet (see text for details). **Left:** each panel corresponds to a different value of the external density power-law index,  $k = 0, 1, 1.5, 2$  where  $\rho_{\text{ext}} = AR^{-k}$ , and shows lightcurves for different viewing angles,  $\theta_{\text{obs}} = 0, 0.2, 0.3, 0.4, 0.6, 0.8, 1, 1.2, \pi/2$ . **Right:** each panel corresponds to a different viewing angle,  $\theta_{\text{obs}} = 0, 0.4, 0.8, \pi/2$  from top to bottom, and shows lightcurves for different values of the external density power-law index,  $k = 0, 1, 1.5, 2$ .

$E_{k,\text{iso}} = E_{53}10^{53}$  erg with  $E_{53} = 1$ , corresponding to a true energy of  $E_{\text{jet}} = (1 - \cos \theta_0)E_{k,\text{iso}} \approx 2 \times 10^{51}$  erg for a double-sided jet.

We consider synchrotron emission from relativistic electrons that are accelerated at the afterglow shock and radiate as they gyrate in the magnetic field within the shocked region. The microphysics processes responsible for magnetic field amplification and particle acceleration are parameterized here by assuming that the magnetic field everywhere in the shocked region holds a fraction  $\epsilon_B = 0.1$  of the local internal energy density in the flow, while the non-thermal electrons just behind the shock hold a fraction  $\epsilon_e = 0.1$  of the internal energy, and have a power-law energy distribution,  $N(\gamma_e) \propto \gamma_e^{-p}$  for  $\gamma_e > \gamma_m$  with  $p = 2.5$ . For more details on the exact form of the spectral emissivity that is used and the calculation of the lightcurves and images see De Colle et al. (2012a,b).

The external density was taken to be a power law with radius,  $\rho_{\text{ext}} = A_k r^{-k}$ . We have made calculations for  $k = 0, 1, 1.5, 2$ , that cover the expected density profiles both for short GRBs, where a uniform ISM ( $k = 0$ ) is expected (in particular for compact binary merger progenitors), and for long GRBs whose immediate circumburst medium is shaped by the stellar wind of their massive star progenitors (e.g., Chevalier & Li, 2000; Ramirez-Ruiz et al. 2001), where  $k = 2$  corresponds to a steady wind, while variations in the wind’s velocity and/or mass loss rate near the end of the massive star’s life could lead to other values of  $k$  (e.g., Garcia-Segura, Langer & Mac Low 1996; Chevalier, Li & Fransson 2004; Ramirez-Ruiz et al. 2005b; van Marle et al. 2006). For example,  $k = 1.4 \pm 0.2$  was inferred for the afterglow of the long and very

bright GRB 130427A (Kouveliotou et al. 2013). The density normalization  $A_k$  for the case  $k = 0$  (a uniform medium) was set to be  $A_0 = \rho_0 = n_{\text{ext}}m_p = 1.67 \times 10^{-24}$  g cm $^{-3}$  corresponding to  $n_0 = n_{\text{ext}}/(1 \text{ cm}^{-3}) = 1$ , while for other  $k$ -values it was set such that the density would be the same at the jet break radius (corresponding approximately to the Sedov radius for a spherical flow with the same true energy; for details see De Colle et al. 2012b). This corresponds to  $A_* \equiv A/(5 \times 10^{11} \text{ gr cm}^{-1}) = 1.65$  for  $k = 2$ .

The radio lightcurves for a wide range of viewing angles  $\theta_{\text{obs}}$  are shown in Fig. 1. Self-absorption is not included (but it is unimportant in the displayed times and frequency). The left panels show lightcurves for a fixed  $k$  and different  $\theta_{\text{obs}}$ , while the right panels show lightcurves for a fixed  $\theta_{\text{obs}}$  and different  $k$ . Figs. 2 and 3 show the afterglow lightcurves in the optical and X-ray, respectively, in the same format as Fig. 1. The on-axis ( $\theta_{\text{obs}} = 0$ ) jet break time is around  $t_j \approx 4 - 5$  days, as can clearly be seen in the on-axis optical and X-ray lightcurves. In the radio the flux still keeps gradually rising after  $t_j$  until the passage of the typical synchrotron frequency  $\nu_m$  through the observed frequency range, after which the flux decays similarly to the optical (Granot et al. 2001).

For off-axis observers ( $\theta_{\text{obs}} > \theta_0$ ), the larger the external density power-law index  $k$  the shallower the rise to the peak of the lightcurve, and the flatter and wider the peak. This more gradual evolution arises since for larger  $k$  it takes a longer time to sweep up the same amount of external mass (for a spherical flow the accumulated swept up mass scales as  $R^{3-k}$ ) that is needed in order for the jet to decelerate down to the same Lorentz factor with the same

associated degree of relativistic beaming of the emitted radiation. For the same reason, the bump in the afterglow lightcurve when the counter-jet becomes visible is much less pronounced for larger  $k$ -values, and it is very hard to clearly see it for  $k = 2$ . This was shown for an on-axis observer ( $\theta_{\text{obs}} = 0$ ) in De Colle et al. (2012b), and here we find that this indeed persists for all  $\theta_{\text{obs}} < \pi/2$  (for  $\theta_{\text{obs}} = \pi/2$  the peak of the emission from the two sides of the jet exactly coincides, as in this case they are both viewed from the same angle, resulting in a single peak).

The effect on the lightcurves of varying  $k$  becomes smaller in the X-ray compared to the optical or radio, since above the cooling break frequency,  $\nu_c$ , the observed flux density  $F_\nu$  becomes much less sensitive to the external density  $\rho_{\text{ext}}$ . We are in the slow cooling regime ( $\nu_m < \nu < \nu_c$ ) so this corresponds to the power-law segment PLS H of the afterglow synchrotron spectrum where  $F_\nu \propto \nu^{-p/2}$  (Sari, Piran & Narayan 1998; Granot & Sari 2002), and for a relativistic self-similar flow (Blandford & McKee 1976)  $F_\nu^{(H)}$  is independent of the external density. Once the flow becomes Newtonian and approaches the spherical Sedov-Taylor solution, there is some dependence of  $F_\nu^{(H)}$  on  $\rho_{\text{ext}}$ . However, it is a rather weak dependence,  $F_\nu^{(H)} \propto \nu^{-p/2} \rho_{\text{ext}}^{-(p-2)/4}$  at a given observed time  $t$ , with an exponent of  $-1/8$  for  $p = 2.5$  or  $-1/20$  for  $p = 2.2$ . For comparison, in PLS G where  $\nu_m < \nu < \nu_c$ ,  $F_\nu^{(G)} \propto \nu^{(1-p)/2} \rho_{\text{ext}}^{1/2}$  for the relativistic spherical phase, and  $F_\nu^{(G)} \propto \nu^{(1-p)/2} \rho_{\text{ext}}^{(19-5p)/20}$  for the Newtonian spherical (Sedov-Taylor), corresponding to an exponent of 0.325 for  $p = 2.5$  or 0.4 for  $p = 2.2$ . For this reason, a wind termination shock where the density switches from  $k = 2$  up to the termination shock radius and then becomes uniform ( $k = 0$ , with a factor of 4 jump in the density at the shock) is hardly seen in PLS H, but in PLS G it is manifested as a flattening of the lightcurve by a factor of  $t^{1/2}$  (Nakar & Granot 2007), which may partly mimic the effect of energy injection.

The bump or flattening in the lightcurve when the counter jet becomes visible can still be seen in the X-ray for  $k = 0$  (and is much harder to see for larger  $k$ -values, similar to the optical or radio), since it arises from relativistic beaming, which is present in all spectral regimes as it is a dynamical effect.

### 3 THE AFTERGLOW IMAGE SIZE, SHAPE AND FLUX CENTROID EVOLUTION

The afterglow image has so far been calculated mainly for a spherical flow (e.g., Waxman 1997; Sari 1998; Panaitescu & Mészáros 1998; Granot, Piran & Sari 1999a,b; Granot 2008; Morsony et al. 2009; van Eerten et al. 2010a). A few works have considered the afterglow images from a GRB jet (e.g., Ioka & Nakamura 2001; Salmonson 2003; Gill & Granot 2018) or the flux centroid motion (e.g. Sari 1999; Ioka & Nakamura 2001; Granot & Loeb 2003), but have used a simple analytic model for the jet dynamics. Here we consider the afterglow images from hydrodynamic simulations of the GRB jet in different external density profiles.

Fig. 4 shows examples of images for two different viewing angles ( $\theta_{\text{obs}} = 0.4, 0.8$ ), and two different external density profiles: a uniform density ( $k = 0$ ) and a (steady) wind-like stratified medium ( $k = 2$ ). The coordinates we use for displaying the afterglow image on the plane of the sky are shown in Fig. 5, and follow section 3.2 of De Colle et al. (2012a). The images are for PLS G ( $\nu_m < \nu < \nu_c$ ), which typically applies to radio frequencies at reasonably late times in which the image may be resolved under favorable conditions. Note that within each PLS the normalized image (i.e. the specific intensity normalized by its mean value

over the entire image,  $I_\nu/\langle I_\nu \rangle$ ) is independent of the observing frequency (e.g. Sari 1998; Granot, Piran & Sari 1999a; Granot & Loeb 2001). The image is symmetric to reflection on the plane containing the jet symmetry axis ( $z$ -axis) and the direction to the observer ( $\tilde{z}$ -axis), i.e.  $\tilde{y} \rightarrow -\tilde{y}$ . The images in Fig. 4 are shown at five different epochs that are indicated by the vertical lines in the relevant panels of Fig. 6, and span times before, during and after the time when the counter-jet becomes visible.

Fig. 4 also shows the location of the central source (thin red plus sign), and the results of a fit to an elliptical Gaussian, where the best fit ellipse is shown in magenta and its center is indicated by a thick magenta plus sign. The motivation for such a fit is that when the image is only marginally resolved (i.e. when its angular size is comparable or slightly smaller than the instrumental beam size) one usually performs a fit to the visibility data of a predetermined functional form such as a circular or an elliptical data, depending on the quality of the data (e.g. Taylor et al. 2005; Taylor & Granot 2006; Pihlström et al. 2007; Mesler et al. 2012). Because of the reflection symmetry,  $\tilde{y} \rightarrow -\tilde{y}$ , the center of the ellipse is along the  $\tilde{x}$ -axis, at  $(\tilde{x}, \tilde{y}) = (\tilde{x}_{\text{el}}, 0)$ , and its semi-major/minor axes are along the  $\tilde{x}$  and  $\tilde{y}$  axes (with lengths or standard deviations  $\sigma_x$  and  $\sigma_y$ , respectively). The model surface brightness that is fit at each observed time is hence  $I_\nu \propto \exp[-(\tilde{x} - \tilde{x}_{\text{el}})^2/2\sigma_x^2 - \tilde{y}^2/2\sigma_y^2]$ .

Finally, Fig. 4 also shows (by a white X sign) the flux centroid's location on the plane of the sky, which is defined as

$$\tilde{\mathbf{r}}_{\text{fc}} = (\tilde{x}_{\text{fc}}, \tilde{y}_{\text{fc}}) = \frac{\int dF_\nu(\tilde{x}, \tilde{y})}{F_\nu} = \frac{\int dF_\nu \tilde{\mathbf{r}}}{\int dF_\nu}, \quad (1)$$

where  $dF_\nu = I_\nu d\Omega = I_\nu d_A^{-2} dS_\perp \propto I_\nu d\tilde{x}d\tilde{y}$ . In our case  $\tilde{y}_{\text{fc}} = 0$  because of the reflection symmetry,  $\tilde{y} \rightarrow -\tilde{y}$ , so that the flux centroid's location is  $\tilde{\mathbf{r}}_{\text{fc}} = (\tilde{x}_{\text{fc}}, 0)$  and fully specified by its  $\tilde{x}$  coordinate,  $\tilde{x}_{\text{fc}}$ .

Fig. 6 shows the evolution of  $\tilde{x}_{\text{fc}}$  and of the best fit parameters for a fit of the surface brightness (or specific intensity  $I_\nu$ ) of the image to an elliptical Gaussian. For  $\theta_{\text{obs}} = 0$ ,  $\tilde{x}_{\text{fc}} = \tilde{x}_{\text{el}} = 0$  where the displayed  $\tilde{x}_{\text{fc}}$ -values show the numerical accuracy, and are a few decades below  $\sigma_x = \sigma_y$ . The fit to an elliptical Gaussian is more reasonable either at early times before the counter-jet becomes visible or shortly after it becomes visible and dominates the observed flux. Before the counter-jet becomes visible the image is dominated by the main jet that points closer to us, and the best fit elliptical Gaussian is centered ( $\tilde{x}_{\text{el}}$ ) near the projection of the front of this jet onto the plane of the sky (as is the flux centroid,  $\tilde{x}_{\text{fc}}$ ), while its semi-major axis is perpendicular to the plane containing the jet axis and our line of sight (i.e. the  $\tilde{y}$  axis;  $\sigma_x > \sigma_y$ ).

Around the time when the counter-jet becomes visible the fluxes from the main jet and counter-jet become comparable, corresponding to two rather compact bright regions in the image that are separated by an angular distance significantly larger than their own angular size. At this stage the fit to an elliptical Gaussian becomes quite poor (an alternative fit to two compact sources may provide a better fit), and the best fit corresponds to an ellipse that is highly elongated along the  $\tilde{y}$  axis ( $\sigma_y \gg \sigma_x$ ), whose major axis  $2\sigma_y$  roughly corresponds to the projected angular separation between the heads of the two jets. The counter-jet is more compact and circular at this stage while the jet pointing closer to us shows a bow-shock like morphology with a somewhat larger angular size. At slightly later times when the counter jet dominates the observed flux, the fit to an elliptical Gaussian improves, and it is centered around the projected location of the counter-jet's head (as is the flux centroid,  $\tilde{x}_{\text{fc}}$ ), and becomes more circular ( $\sigma_y \approx \sigma_x$ ).

Comparing the images for  $k = 0$  and  $k = 2$  corresponding to the same  $\theta_{\text{obs}}$  and a similar flux ratio between the main jet and

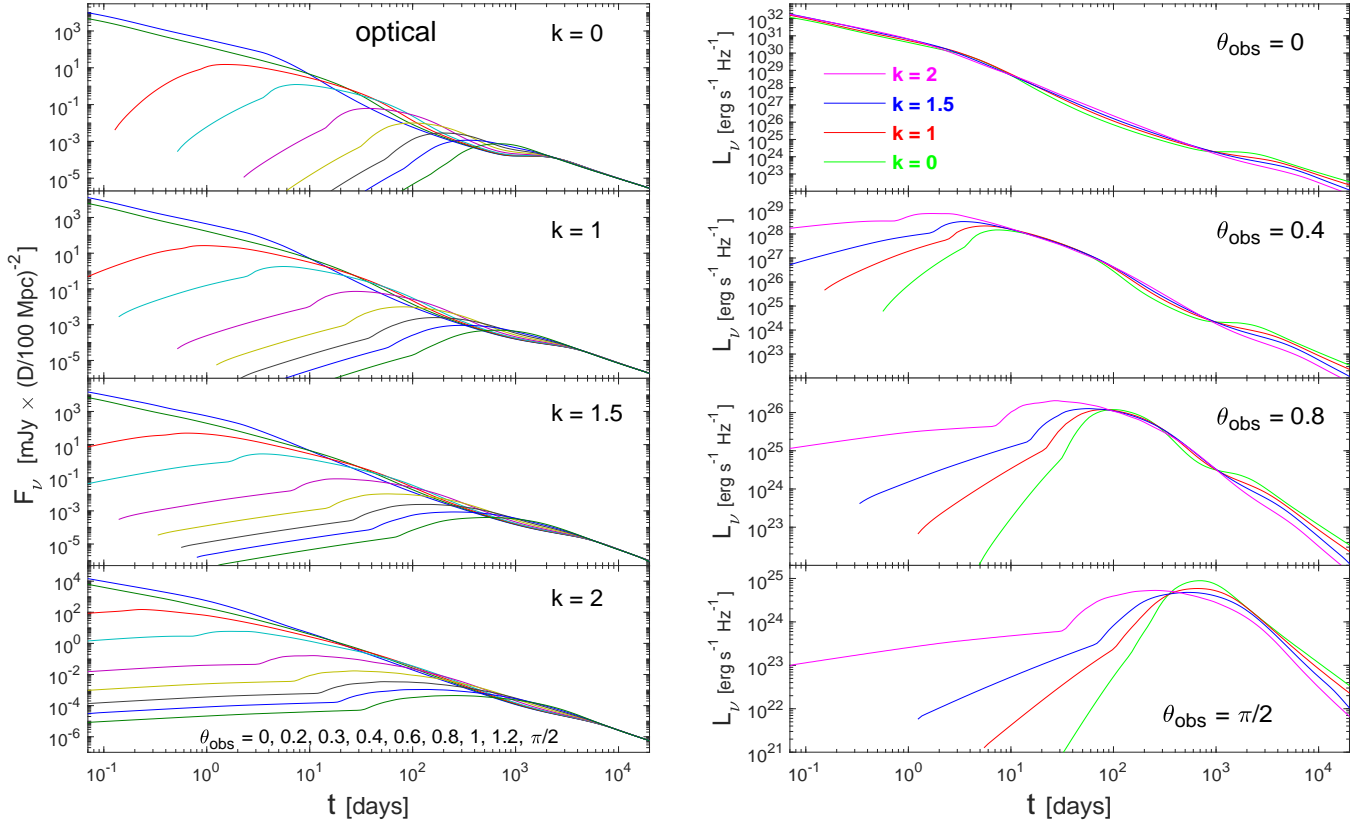


Figure 2. Optical (left;  $\nu = 4.56 \times 10^{14}$  Hz, R-band) afterglow light curves, in the same format as Fig. 1.

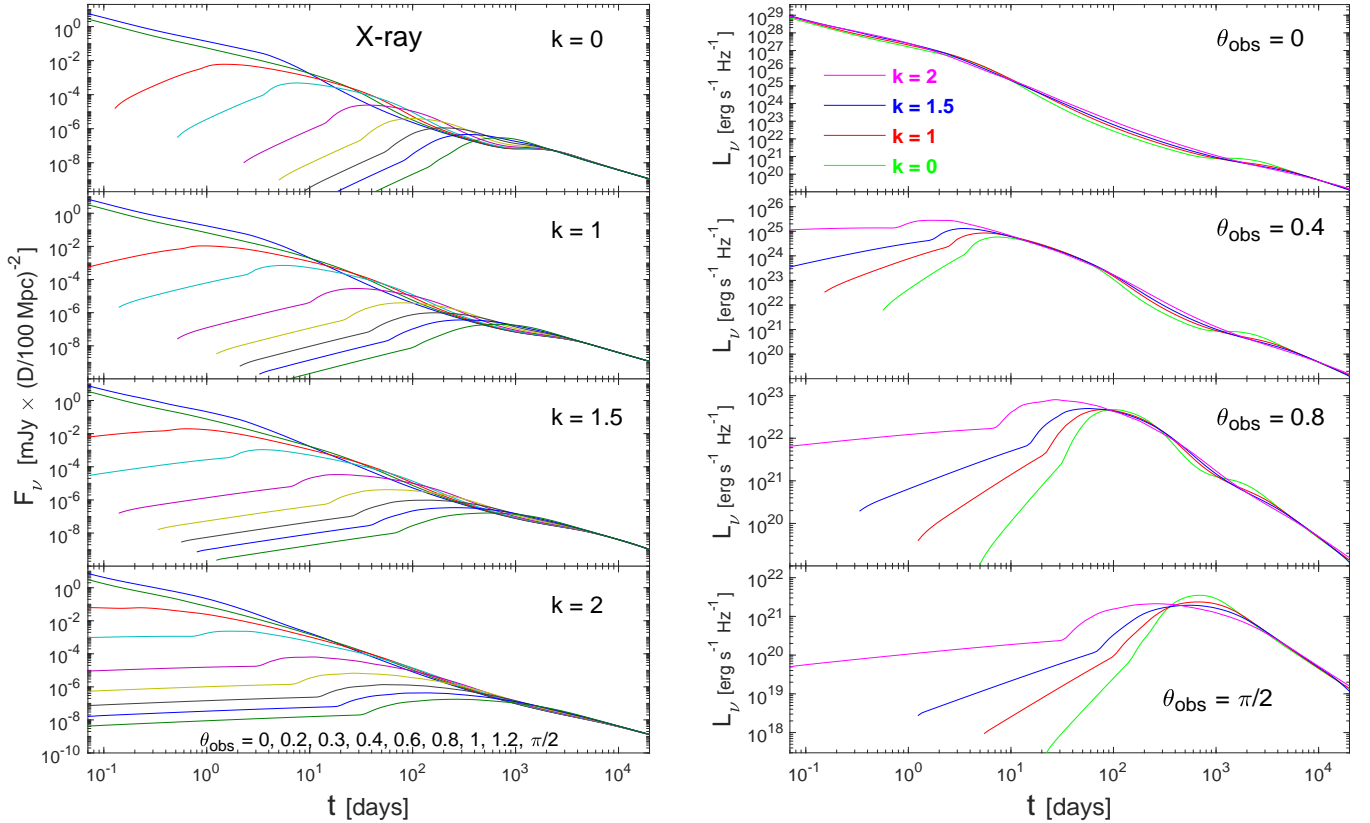
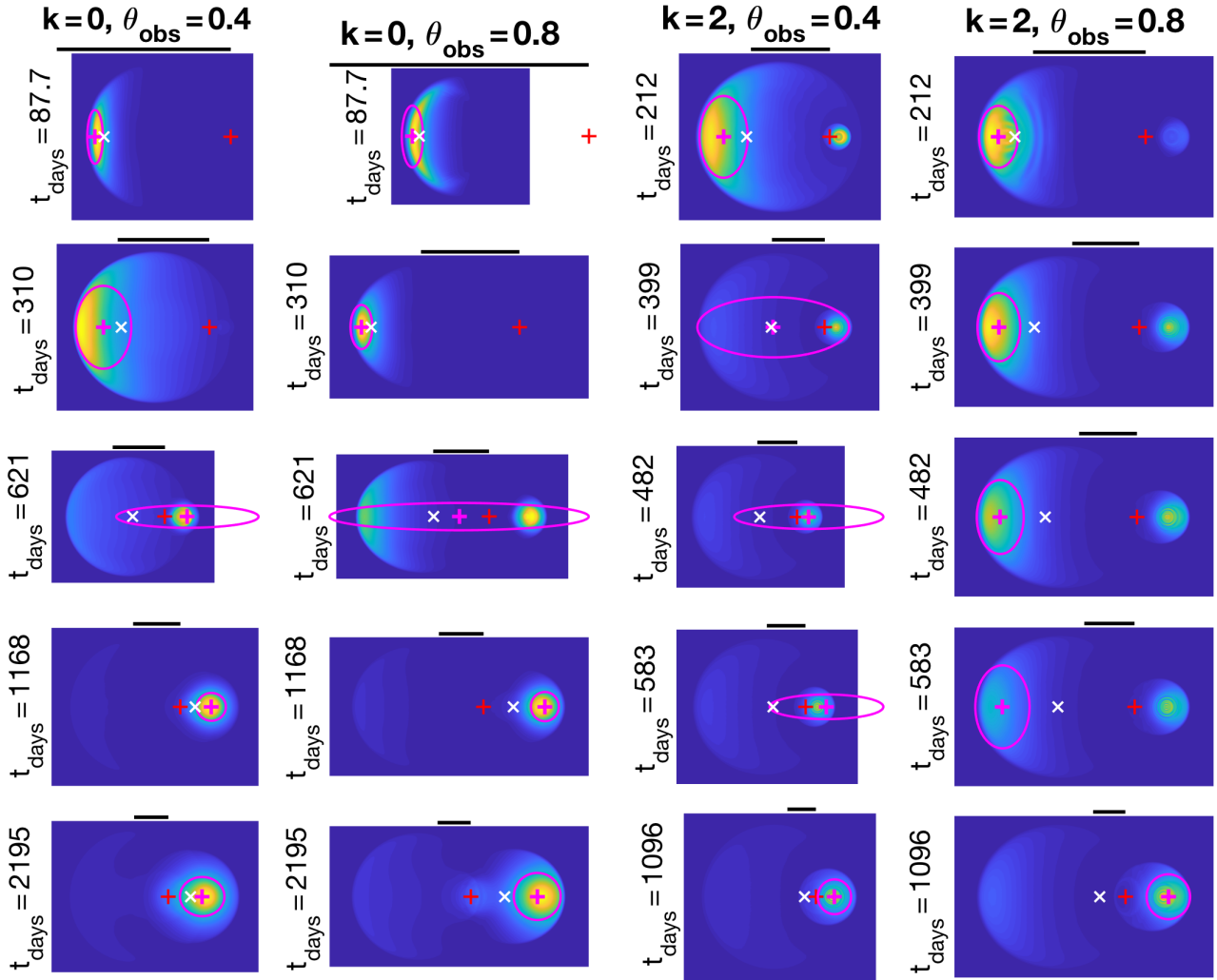


Figure 3. X-ray (right;  $h\nu = 1$  keV,  $\nu = 2.42 \times 10^{17}$  Hz) afterglow light curves, in the same format as Fig. 1.



**Figure 4.** Radio images (in PLS G,  $v_m < v < v_c$ ) for  $k = 0$  (columns 1 and 2, from the left) and  $k = 2$  (columns 3 and 4), for  $\theta_{\text{obs}} = 0.4$  (columns 1 and 3) and  $\theta_{\text{obs}} = 0.8$  (columns 2 and 4), for five different observed times (rows 1 to 5). The thin red plus sign is the location of the central source. The thin white X sign is the location of the flux centroid. The magenta ellipse whose center is the thick magenta plus sign is the best fit elliptical Gaussian to the image. The thick black line above each panel is a yardstick of length  $10^{18}$  cm. Under a rescaling of the energy and  $A_k$  by factors of  $\zeta = E_{53}$  and  $a$ , respectively, the yardstick's length becomes  $\alpha \times 10^{18}$  cm where  $\alpha = (E_{53}/a)^{1/(3-k)}$ , and the observed time of the image becomes  $\alpha$  times that indicated in the figure (see § 4 for details).

counter-jet, it appears that the best fit ellipse has a smaller axis ratio for  $k = 2$  compared to  $k = 0$ , corresponding to a somewhat less elongated and rounder image. This trend is consistent with the images for the spherical self-similar relativistic phase in which the effective width of the emitting shell of shocked external medium behind the afterglow shock increases with  $k$  (Blandford & McKee 1976; De Colle et al. 2012a), resulting in a more uniform and less limb-brightened image (Granot & Loeb 2001; Granot 2008).

The relatively rapid transition between the flux being dominated by the main jet and the counter-jet results in a rather fast motion of the flux centroid  $\tilde{x}_{\text{fc}}$ , as can clearly be seen in Fig. 6, especially in the bottom panels. The maximal displacement of the flux centroid from the projected location of the central source,  $\tilde{x}_{\text{max}} = \max(|\tilde{x}_{\text{fc}}|)$ , or the flux centroid's total motion,  $\Delta\tilde{x}_{\text{fc}}$ , are expected to be of the order of the jet's (core) non-relativistic transition radius,  $R_{\text{NR}}$ , for large viewing angles  $\theta_{\text{obs}} \approx 1$ . It decreases for smaller viewing angles due to the projection effect, such that

$$\tilde{x}_{\text{max}}(\theta_{\text{obs}} < 1) \approx R_{\text{NR}} \sin \theta_{\text{obs}}. \quad (2)$$

For the largest viewing angles,  $\theta_{\text{obs}} \approx \pi/2$  ( $\theta_{\text{obs}} = \pi/2$ ),  $\Delta\tilde{x}_{\text{fc}}$  decreases (vanishes) since in that case the two jets have rather similar (equal) fluxes and projected displacements around the non-relativistic transition time, which causes the flux centroid to be closer to (exactly at) the projected location of the central source.

A more delicate question is how to best estimate  $R_{\text{NR}}$  (e.g. Granot & Loeb 2003; Granot, Ramirez-Ruiz & Loeb 2005; Wygoda, Waxman & Frail 2011; Granot & Piran 2012; De Colle et al. 2012b). Assuming the jet spreads sideways exponentially once  $\Gamma < \theta_0^{-1}$  at  $R > R_j$  leads to

$$R_{\text{NR},1} \approx (1 - \ln \theta_0) R_j, \quad (3)$$

$$R_j = \left[ \frac{(3-k)E_{\text{jet}}}{2\pi A c^2} \right]^{1/(3-k)} = 2^{1/(3-k)} R_S(E_{\text{jet}}) \quad (4)$$

$$= \begin{cases} 8.59 \times 10^{17} E_{\text{jet},51.3}^{1/3} n_0^{-1/3} \text{ cm} & (k=0), \\ 7.06 \times 10^{17} E_{\text{jet},51.3} A_*^{-1} \text{ cm} & (k=2), \end{cases}$$

where  $R_j$  is the jet break radius,  $E_{\text{jet},51.3} = E_{\text{jet}}/(2 \times 10^{51} \text{ erg})$  and

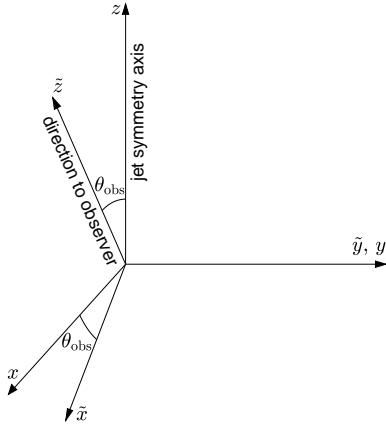


**Figure 5.** A diagram of the coordinates we use. The  $z$ -axis is the jet’s symmetry axis, while the  $\tilde{z}$ -axis points to the observer and is in the  $x$ - $z$  plane at an angle of  $\theta_{\text{obs}}$  from the  $z$ -axis. The  $y$  and  $\tilde{y}$  axes coincide. The afterglow image is in the plane of the sky, i.e. in the  $\tilde{x}$ - $\tilde{y}$  plane.

$R_S(E_{\text{jet}})$  is the Sedov radius corresponding to the jet’s true energy. If, on the other hand, one neglects the jet’s lateral spreading (which numerical simulations suggest to be modest for  $\theta_0 \gtrsim 0.1 - 0.2$ ) and assumes it continues to evolve as if it were part of a spherical flow even after the jet break time, until it becomes non-relativistic then  $R_{\text{NR}} = R_S(E_{k,\text{iso}})$  corresponds to the Sedov radius for the jet’s isotropic equivalent energy,

$$R_{\text{NR},2} = \left[ \frac{(3-k)E_{k,\text{iso}}}{4\pi A c^2} \right]^{\frac{1}{3-k}} = \begin{cases} 2.51 \times 10^{18} E_{53}^{1/3} n_0^{-1/3} \text{ cm} & (k=0), \\ 1.77 \times 10^{19} E_{53} A_*^{-1} \text{ cm} & (k=2). \end{cases} \quad (5)$$

Judging from the jet’s dynamics in hydrodynamic simulations (see, e.g., Figs. 4 and 5 of De Colle et al. 2012b), and estimating  $R_{\text{NR}}$  by the jet’s radius when its energy weighted mean proper velocity  $u = \Gamma\beta$  equals unity, it appear to be closer to  $R_{\text{NR},1}$  than to  $R_{\text{NR},2}$ . From our calculated  $\tilde{x}_{\text{max}} = \max(|\tilde{x}_{\text{fc}}|)$  for  $k=0$  we infer  $\tilde{x}_{\text{max}}/R_{\text{NR},1} \sin \theta_{\text{obs}} = 1.12$  and  $1.01$  while  $\tilde{x}_{\text{max}}/R_{\text{NR},2} \sin \theta_{\text{obs}} = 1.00$  and  $0.90$ , for  $\theta_{\text{obs}} = 0.4$  and  $0.8$ , respectively, showing a similarly good agreement. However, for  $k=2$  we obtain  $\tilde{x}_{\text{max}}/R_{\text{NR},1} \sin \theta_{\text{obs}} = 2.47$  and  $1.99$  while  $\tilde{x}_{\text{max}}/R_{\text{NR},2} \sin \theta_{\text{obs}} = 0.099$  and  $0.079$ , for  $\theta_{\text{obs}} = 0.4$  and  $0.8$ , respectively, implying a poorer agreement, and a better match for  $R_{\text{NR},1}$ . A better agreement, good to  $\sim 10\%$ , is obtained when using

$$R_{\text{NR}} = R_{\text{NR},1}^f R_{\text{NR},2}^{1-f} \quad \text{with} \quad f \approx 0.75. \quad (6)$$

Note the stronger dependence of  $\Delta \tilde{x}_{\text{fc}} \sim \tilde{x}_{\text{max}} \propto R_{\text{NR}}$  (and the corresponding angular scale that is discussed next) on  $E_{k,\text{iso}}$  or  $E_{\text{jet}}$  and on the external density normalization  $A$  for larger  $k$ -values.

The angular size of the image around the time of the peak in the lightcurve for a given  $\theta_{\text{obs}}$  also scales as  $R_{\text{NR}}$ , and becomes comparable to  $\tilde{x}_{\text{max}} \sim \Delta \tilde{x}_{\text{fc}}$  around the time when the counter jet becomes visible and its flux becomes comparable to that of the main jet. The corresponding typical angular scale assuming a relatively low redshift source at a distance of  $D = 100 D_{100}$  Mpc, which may

potentially be resolved is (e.g. Granot & Loeb 2003), is

$$\theta_{\text{NR}} = \frac{R_{\text{NR}}}{D} = \begin{cases} 1.54 g_{0.2} \theta_{0.2}^{-1/6} E_{\text{jet},51.3}^{1/3} n_0^{-1/3} D_{100}^{-1} \text{ mas} & (k=0), \\ 1.67 g_{0.2} \theta_{0.2}^{-1/2} E_{\text{jet},51.3} A_*^{-1} D_{100}^{-1} \text{ mas} & (k=2), \\ 1.54 g_{0.2} \theta_{0.2}^{1/2} E_{53}^{1/3} n_0^{-1/3} D_{100}^{-1} \text{ mas} & (k=0), \\ 1.67 g_{0.2} \theta_{0.2}^{3/2} E_{53} A_*^{-1} D_{100}^{-1} \text{ mas} & (k=2), \end{cases} \quad (7)$$

where  $g_{0.2} = [(1 - \ln \theta_0)/(1 - \ln 0.2)]^{0.75}$ ,  $\theta_{0.2} = \theta_0/0.2$ , and we have used Eq. (6). For comparison, the Very Long Baseline Array (VLBA) has an angular resolution of  $\sim 170 \mu\text{as}$  at 43 GHz, and may potentially resolve the jet around the time of the peak in the lightcurve for binary mergers that are detectable in gravitational waves by advanced LIGO/VIRGO.

#### 4 SCALING WITH MODEL PARAMETERS AND DEGENERACIES

Inferring all of the model parameters from detailed fits to afterglow data is usually a challenging task, even when elaborate observations are available, due to the rather large number of model free parameters, and degeneracies between them. Nonetheless, for well monitored afterglows some of the keys model parameters can be inferred reasonably well, such as the electron power-law index  $p$ , which can be derived from the spectral slope in PLSs G or H. Ideally, for an on-axis observer the temporal decay index in the same PLS (for a spherical flow or before the jet break time) could then help determine the external density power-law index,  $k$ . Then, the parameters  $\epsilon_e$ ,  $\epsilon_B$ ,  $E_{k,\text{iso}}$ , and the external density normalization  $A$  can be determined by the flux normalization  $F_{v,\text{max}}$  and three break frequencies  $\nu_{sa}$ ,  $\nu_m$  and  $\nu_c$  (e.g. Wijers & Galama 1999; Sari & Esin 2001; Granot, Ramirez-Ruiz & Loeb 2005), up to the degeneracy pointed out by Eichler & Waxman (2005). The latter degeneracy arises from the uncertainty on the fraction  $\xi_e$  of the post-shock accelerated electrons that take part in the power-law energy distribution that emits the synchrotron radiation we observe. For a jet there are additional free parameters, namely our viewing angle  $\theta_{\text{obs}}$  relative to the jet’s symmetry axis, and parameters that describe its initial angular structure (its initial half-opening angle  $\theta_0$  for a top-hat jet, and usually more parameters for other jet structures).

In practice, even in some very well monitored afterglows and when we have good reason to expect  $k=0$ , such as for the short GRB 170817A/GW 170817, a lot of degeneracy still remains even after a very detailed fit to the afterglow lightcurves at all observed frequencies. For this reason imaging becomes a very important diagnostic tool that may potentially help to break such a degeneracy (e.g., Gill & Granot 2018; Nakar & Piran 2018; Nakar et al. 2018).

Fitting afterglow data to the results of numerical calculations based on hydrodynamical simulations of the GRB jet during the afterglow phase becomes much more efficient numerically when taking advantage of the relevant scaling relations (e.g. Granot 2012; van Eerten, van der Horst & MacFadyen 2012; van Eerten & MacFadyen 2012a). This scaling ultimately arises from the freedom in the choice of the three basic physical units (of mass, length and time) when applying the results of a numerical simulation to the relevant physical system (Granot 2012). Relativistic hydrodynamic (or magneto-hydrodynamic; MHD) simulations must preserve the value of the speed of light in vacuum  $c$  (a universal dimensional constant), requiring the scaling factors of length and time to be equal, thus leaving two free parameters for rescaling

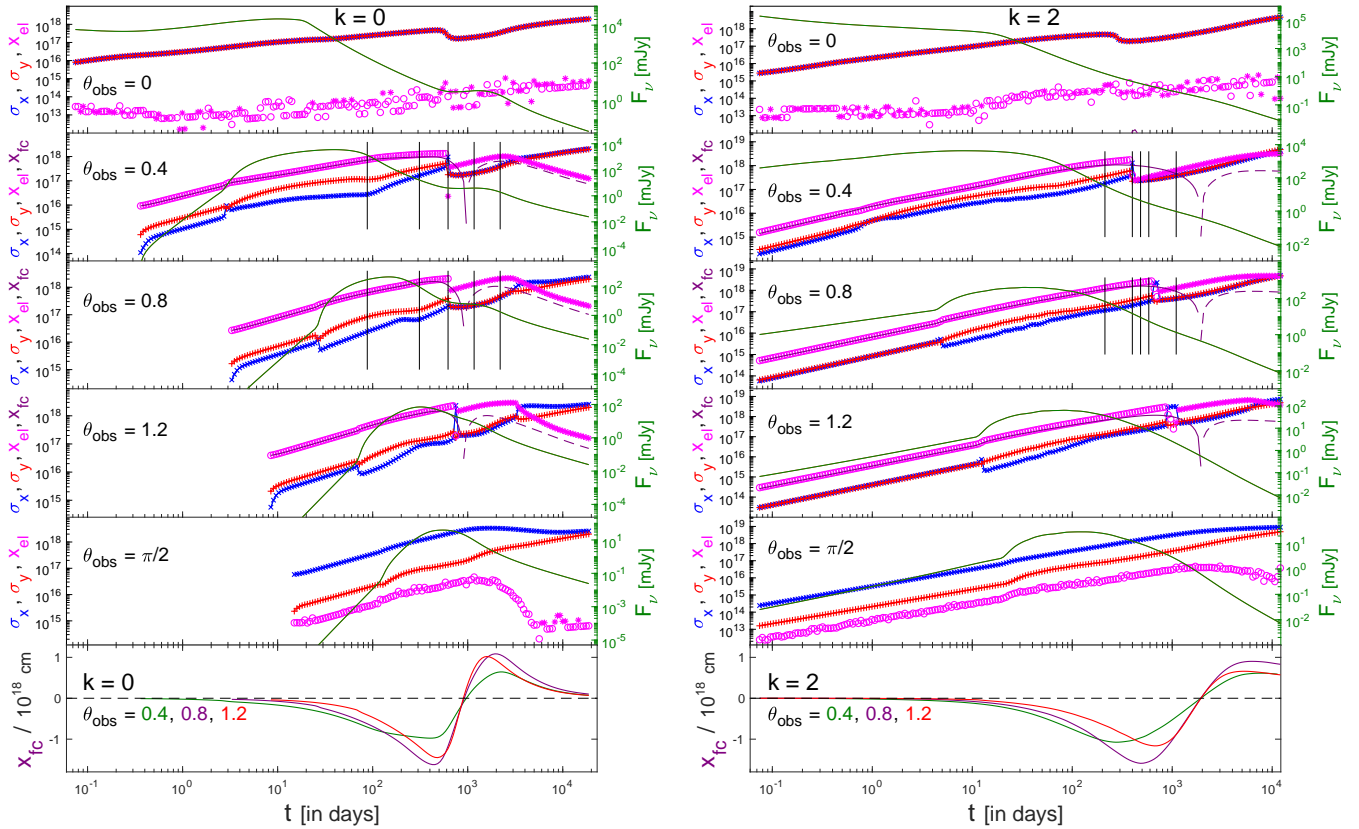


**Figure 6.** Properties of the radio image observed from different viewing angles ( $\theta_{\text{obs}} = 0, 0.4, 0.8, 1.2, \pi/2$ ), for  $k = 0$  (left) and  $k = 2$  (right). The flux density (right y-axis) is for  $\nu = 8.46$  GHz and a distance of 100 Mpc, while the normalized image ( $I_\nu / \langle I_\nu \rangle$ ) holds for any frequency in PLS G, where  $F_\nu \propto \nu^{(1-p)/2}$ . An elliptical Gaussian to the image is shown in terms of its best fit parameters: the location of the ellipse’s center,  $\bar{x}_{\text{el}}$  (in magenta;  $\bar{x}_{\text{el}} > 0$  values are denoted by an asterisk, while  $|\bar{x}_{\text{el}}|$  for  $\bar{x}_{\text{el}} < 0$  values is denoted by a circle), and its semi-axes  $\sigma_x$  (it blue  $x$ ’s) and  $\sigma_y$  (red  $+$ ’s). The symmetry of the problem implies  $\bar{y}_{\text{el}} = \bar{y}_{\text{fc}} = 0$ . Also shown as a useful reference are the radio lightcurves (in dark green solid lines, using the right y-axis). The vertical thin solid black lines in the second ( $\theta_{\text{obs}} = 0.4$ ) and third ( $\theta_{\text{obs}} = 0.8$ ) panels indicate the observed times for which the images are shown in Fig. 4. The location of the flux centroid,  $\bar{x}_{\text{fc}}$  (measured in cm; see Fig. 5), is shown in deep purple ( $\bar{x}_{\text{fc}} > 0$  values are shown by the solid line while  $|\bar{x}_{\text{fc}}|$  for  $\bar{x}_{\text{fc}} < 0$  values is shown by the dashed line). In the bottom panels  $\bar{x}_{\text{fc}}$  is shown with a linear y-axis (for  $\theta_{\text{obs}} = 0, \pi/2$  one has  $\bar{x}_{\text{fc}} = 0$  due to symmetry).

simulation results:  $\alpha = t'/t = l'/l$  and  $\zeta = m'/m$  when rescaling to primed units and quantities (see Granot 2012, for details). Instead of using the scaling factors of the basic physical units, one can conveniently use those for useful physical quantities such as the energy  $\kappa = E'/E = m'/m = \zeta$  and proper rest mass density  $\lambda = \rho'/\rho = \zeta/\alpha^3$  (e.g. van Eerten, van der Horst & MacFadyen 2012; van Eerten & MacFadyen 2012a).

In our case it may be more convenient to rescale the external density normalization factor  $a = A'_k/A_k = \zeta/\alpha^{3-k} = \lambda^{(3-k)/3} \kappa^{k/3}$  and energy  $\zeta = \kappa = E'/E$ . In this case length and time scale by a factor  $\alpha = (\zeta/a)^{1/(3-k)} = (\kappa/\lambda)^{1/3}$ . This can be seen in Eqs. (3)–(5) where the critical radii and in particular  $R_{\text{NR}}$  scale as  $(E/A)^{1/(3-k)}$ . Since  $R'(t' = \alpha t) = \alpha R(t)$  one can conveniently normalize the lengths and times by  $R_{\text{NR}}$  and  $t_{\text{NR}} = R_{\text{NR}}/c$ , respectively,  $\bar{t} = t/t_{\text{NR}}$  and  $\bar{l} = l/R_{\text{NR}}$ . In these normalized units the size and shape of the image at any given observed time (as well as the normalized surface brightness distribution within the image at any given spectral PLS), and in particular the ones that are shown in Fig. 4 are valid for any rescaling of the energy ( $\zeta$ ) and the external density normalization factor ( $a$ ), which only affect  $R_{\text{NR}} = ct_{\text{NR}} \propto (E/A)^{1/(3-k)}$ . Therefore, measurements of the image size can help constrain  $E/A$ .

While the scaling factor  $\alpha$  of length and time depends only on the ratio of the scaling factors,  $\zeta/a$ , the scaling of the flux den-

sity  $F_\nu$  within each spectral PLS depends on each of the scaling factors separately, where the dependence changes between different PLSs (for the explicit scalings see Granot 2012; van Eerten & MacFadyen 2012a). Note that within each PLS the usual dependence on the shock microphysics parameters ( $\epsilon_e, \epsilon_B, \xi_e, p$ ) remains valid (e.g. Granot & Sari 2002; van Eerten & MacFadyen 2012a; Granot 2012). For any rescaling by factors ( $\zeta, a$ ), within each PLS  $t$  scales by a factor  $\alpha = (\zeta/a)^{1/(3-k)}$  while  $F_\nu$  scales by another PLS-dependent factor. In a log-log plot of  $F_\nu(t)$  this corresponds to horizontal and vertical shifts of the lightcurve, along the time and flux density axes, respectively, while its shape does not change. The lightcurve shape depends on the dynamics, namely on the external density power-law index,  $k$ , and the jet angular structure, which may make it possible to constrain  $k$ , even when some degeneracy remains in the other model parameters.

The scaling of  $F_\nu$  implies that the mean surface brightness within the image,  $\langle I_\nu \rangle$ , must also scale correspondingly ( $\langle I_\nu \rangle \propto F_\nu/S_\perp$  where  $S_\perp \propto l^2$  is the area of the image on the plane of the sky, such that  $S'_\perp/S_\perp = \alpha^2$ ), and has the same frequency dependence as  $F_\nu$  within any given PLS. However, within each PLS the normalized surface brightness,  $I_\nu / \langle I_\nu \rangle$ , as a function of the normalized location within the image at any given normalized time,  $[\bar{x}(\bar{t}), \bar{y}(\bar{t})]/R_{\text{NR}}$ , remains invariant under any rescaling by factors

( $\zeta, a$ ). All of the scalings mentioned above make our results applicable to a wide range of parameter space.

## 5 DISCUSSION

Off-axis lightcurves from 2D relativistic hydrodynamic simulations have been presented for different viewing angles  $\theta_{\text{obs}}$  with respect to the symmetry axis of a jet propagating into a power-law external density profile,  $\rho_{\text{ext}} \propto R^{-k}$  for  $k = 0, 1, 1.5, 2$ , ranging from a uniform ISM-like medium ( $k = 0$ ) that is expected for short GRBs, to a stratified (steady) wind-like medium ( $k = 2$ ) that may be expected from the massive star progenitors of long GRBs. The lightcurves were calculated in the radio, optical and X-ray, as such orphan afterglows may be detected in upcoming surveys covering different parts of the electromagnetic spectrum. It was found that for off-axis observers ( $\theta_{\text{obs}} > \theta_0$ ) a larger  $k$  results in a shallower the rise to the peak of the lightcurve with the flatter and wider the peak, leading to a much less pronounced bump in the afterglow lightcurve when the counter-jet becomes visible that hard to clearly observe for  $k = 2$ .

This may potentially partly explain the lack of a clear counter-jet induced bump in the late afterglow lightcurves of long GRBs, for which  $1 \lesssim k \lesssim 2$  may be expected. For the longest GRB afterglow monitored in the radio, GRB 030329, it is not clear how well such an explanation for the lack of a clear flattening or rebrightening (e.g. Pihlström et al. 2007; Mesler et al. 2012) might work, since in that case detailed afterglow modeling favors a uniform external density ( $k = 0$ ; van der Horst et al. 2008). It is worth noting, however, that for nearby NS-NS or NS-BH mergers that are detected in gravitational waves and are accompanied by long-lived afterglow emission, a uniform external medium is expected ( $k = 0$ ), which may help in detecting a late time flattening or rebrightening in the lightcurve corresponding to the contribution from the counter-jet. It would be useful to search for such a signal, which may help probe the structure of the outflow from such events, and the symmetry between the main jet and counter jet, and/or the external density that they are expanding into.

The corresponding afterglow images were also calculated in the radio, as that is where the best angular resolution is currently available, using very large baseline interferometry (VLBI; see the discussion around Eq. (7)). In particular, the observed size and shape of the radio afterglow image were calculated along with the motion of its flux centroid, which may be measured even in some cases when the image itself is not resolved. Fits of the image to an elliptical Gaussian were also performed, since they are often done by observers when the image is only marginally resolved, and their detailed properties were discussed.

These detailed properties of the afterglow lightcurves and image may help to clearly distinguish orphan GRB afterglows from other types of transients in upcoming surveys, which may otherwise prove to be very challenging. In particular, this may help identify relativistic jets that are pointed away from us, either in nearby supernovae Ib/c (some of which have been associated with long duration GRBs) for which  $1 \lesssim k \lesssim 2$  may be expected, or in nearby binary neutron star mergers that are detected through their gravitational wave signal, and may also produce short duration GRBs at least for some viewing angles (as in the case of GW 170827/GRB 170817A). It is most promising to detect or angularly resolve such transients near the time of the peak in their lightcurve. which for large viewing angles corresponds to a Lorentz factor  $\Gamma \lesssim$  a few. Therefore, most of the results in this work are applicable also for moderately relativistic jets with a modest initial

Lorentz factor of  $\Gamma_0 \gtrsim$  a few, which may be intrinsically much more common than ultra-relativistic jets ( $\Gamma_0 \gg 1$  or  $\Gamma_0 \gtrsim 100$  that are often inferred for GRBs).

## ACKNOWLEDGEMENTS

J.G. is supported by the Israeli Science Foundation under grant No. 719/14. FDC acknowledges support from the UNAM-PAPIIT grant IN117917. ER-R is supported in part by David and Lucile Packard Foundation and the Niels Bohr Professorship from the DNRFF. We acknowledge the support from the Miztli-UNAM supercomputer (project LANCAD-UNAM-DGTIC-281) in which the simulations were performed.

## REFERENCES

- Abbott, B. P., et al. 2017a, PhRvL, 119, 161101  
 Abbott, B. P., et al. 2017b, ApJL, 848, L12  
 Abbott, B. P., et al. 2017c, ApJL, 848, L13  
 Bietenholz, M. F., et al. 2010, ApJ, 725, 4  
 Bietenholz, M. F., De Colle, F., Granot, J., Bartel, N., & Soderberg, A. M. 2014, MNRAS, 440, 821  
 Blandford, R. D. & McKee, C. F. 1976, Phys. Fluids, 19, 1130  
 Chevalier, R. A. & Li, Z.-Y. 2000, ApJ, 536, 195  
 Chevalier, R. A., Li, Z.-Y., & Fransson, C., 2004, ApJ, 606, 369  
 De Colle, F., Kumar, P., & Aguilera-Dena, D. R. 2018, arXiv:1803.00602  
 De Colle, F., Granot, J., Lopez-Camara, D., & Ramirez-Ruiz, E. 2012a, ApJ, 746, 122  
 De Colle, F., Ramirez-Ruiz, E., Granot, J., & Lopez-Camara, D. 2012b, ApJ, 751, 57  
 Drout, M. R., Piro, et al. 2017, Sci, 358, 1570  
 Duffell, P. C., Quataert, E., & MacFadyen, A. I. 2015, ApJ, 813, 64  
 Eichler, D., & Granot, J. 2006, ApJ, 641, L5  
 Eichler, D., & Waxman, E. 2005, ApJ, 627, 861  
 Gal-Yam, A., et al. 2006, ApJ, 639, 331  
 Garcia-Segura, G., Langer, N., & Mac Low, M.-M. 1996, A&A, 316, 133  
 Ghirlanda, G., et al. 2014, PASA, 31, 22  
 Gill, R., & Granot, J. 2018, MNRAS (DOI:10.1093/mnras/sty1214)  
 Goldstein, A., et al., 2017, ApJ, 848, L14  
 Granot, J. 2005, ApJ, 631, 1022  
 Granot J., 2007, Rev. Mex. Astron. Astrofis., 27, 140  
 Granot, J. 2008, MNRAS, 390, L46  
 Granot, J. 2012, MNRAS, 421, 2610  
 Granot, J., & Kumar, P. 2003, ApJ, 591, 1086  
 Granot, J., & Loeb, A. 2001, ApJ, 551, L63  
 Granot, J., & Loeb, A. 2003, ApJ, 593, L81  
 Granot J., Miller M., Piran T., Suen W. M., & Hughes P. A. 2001, in Costa E., Frontera F., Hjorth J., eds, GRBs in the Afterglow Era. Springer-Verlag, Berlin, p. 312  
 Granot, J., Panaitescu, A., Kumar, P., & Woosley, S. E. 2002, ApJ, 570, L61  
 Granot, J., & Piran, T. 2012, MNRAS, 421, 570  
 Granot, J., Piran, T., & Sari, R. 1999a, ApJ, 513, 679  
 Granot J., Piran T., & Sari R. 1999b, ApJ, 527, 236  
 Granot, J., & Ramirez-Ruiz, E. 2004, ApJ, 609, L9  
 Granot, J., & Ramirez-Ruiz, E. 2012, “Jets and gamma-ray burst unification schemes”, chap. 11 “Gamma-ray bursts”, Eds.: C. Kouveliotou, S. E. Woosley, & R. A. M. J. Wijers; Cambridge University Press.  
 Granot, J., Ramirez-Ruiz, E. & Loeb, A. 2005, ApJ, 618, 413  
 Granot, J., & Sari, R. 2002, ApJ, 568, 820  
 Haggard D., Nynka M., Ruan J. J., Kalogera V., Cenko S. B., Evans P., Kennea J. A., 2017, ApJ, 848, L25  
 Hallinan, G., et al. 2017, Sci, 358, 1579  
 Huang, Y. F., Dai, Z. G., & Lu, T. 2002, MNRAS, 332, 735  
 Ioka, K., & Nakamura, T. 2001, ApJ, 561, 703  
 Kouveliotou, C., Granot, J., Racusin, J., et al. 2013, ApJ, 779, L1

- Kumar, P., & Granot, J. 2003, *ApJ*, 591, 1075
- Lamb, G. P., & Kobayashi, S. 2017, *MNRAS*, 472, 4953
- Lamb, Gavin P., & Kobayashi, S. 2008, *MNRAS*, 478, 733
- Lamb, G. P., Tanaka, M., & Kobayashi, S. 2018, *MNRAS*, 476, 4435
- Lazzati, D., Deich, A., Morsony, B. J., & Workman, J. C. 2017, *MNRAS*, 471, 1652
- Lazzati, D., Lúpez-Cǧmara, D., Cantiello, M., Morsony, B. J., Perna, R., & Workman, J. C. 2017, *ApJ*, 848, L6
- Lazzati, D., Perna, R., Morsony, B. J., Lúpez-Cǧmara, D., Cantiello, M., Ciolfi, R., Giacomazzo, & B., Workman, J. C. 2018, *PRL*, 120, 241103
- Levinson, A., Ofek, E. O., Waxman, E., & Gal-Yam, A. 2002, *ApJ*, 576, 923
- Lyman J. D., et al., 2018, preprint, (arXiv:1801.02669)
- Murguía-Berthier, A., Montes, G., Ramirez-Ruiz, E., De Colle, F., Lee, W. H. 2014, *ApJ*, 788, L8
- Murguía-Berthier, A., et al. 2017, *ApJ*, 835, L34
- Margutti R., et al., 2017, *ApJ*, 848, L20
- Margutti R., et al., 2018, *ApJ*, 856, L18
- Mesler, R. A., Pihlström, Y. M., Taylor, G. B., & Granot, J. 2012, *ApJ*, 759, 4
- Mészáros, P., Rees, M. J., & Wijers, R. A. M. J. 1998, *ApJ*, 499, 301
- Mooley, K. P., et al. 2018, *Natur*, 554, 207
- Morsony, B. J., Workman, J. C., Lazzati, D., Medvedev, M. V. 2009, *MNRAS*, 392, 1397
- Nagakura, H., Hotokezaka, K., Sekiguchi, Y., Shibata, M., & Ioka, K. 2014, *ApJ*, 784, L28
- Nakar, E., Gottlieb, O., Piran, T., Kasliwal, M. M., & Hallinan, G. 2018, preprint (arXiv:1803.07595)
- Nakar, E., & Granot, J. 2007, *MNRAS*, 380, 1744
- Nakar, E., & Piran, T. 2003, *NewA*, 8, 141
- Nakar, E., & Piran, T. 2018, *MNRAS*, 478, 407
- Nakar, E., Piran, T., & Granot, J. 2002, *ApJ*, 579, 699
- Panaiteescu, A., & Mészáros P., 1998, *ApJ*, 493, L31
- Panaiteescu, A., & Mészáros P., 1999, *ApJ*, 526, 707
- Pihlström, Y. M., Taylor, G. B., Granot, J., & Doeleman, S. 2007, *ApJ*, 664, 411
- Ramirez-Ruiz, E., Granot, J., Kouveliotou, C., Woosley, S. E., Patel, S. K., & Mazzali, P. A. 2005, *ApJ*, 625, L91
- Ramirez-Ruiz, E., Dray, L. M., Madau, P., & Tout, C. A. 2001, *MNRAS*, 327, 829
- Ramirez-Ruiz, E., García-Segura, G., Salmonson, J. D., & Pérez-Rendón, B., 2005, *ApJ*, 631, 435
- Rezzolla, L., Giacomazzo, B., Baiotti, L., Granot, J., Kouveliotou, C., & Aloy, M. A. 2011, *ApJ*, 732, L6
- Rhoads, J. E. 1997, *ApJ*, 487, L1
- Rhoads, J. E. 1999, *ApJ*, 525, 737
- Rhoads, J. E. 2003, *ApJ*, 591, 1097
- Rossi, E., Lazzati, D., & Rees, M. J. 2002, *MNRAS*, 332, 945
- Rossi, E. M., Perna, R., & Daigne, F. 2008, *MNRAS*, 390, 675
- Ruan, J. J., Nynka, M., Haggard, D., Kalogera, V., & Evans, P. 2018, *ApJ*, 853, L4
- Ruiz, M., Lang, R. N., Paschalidis, V., & Shapiro, S. L. 2016, *ApJ*, 824, L6
- Ryan, G., van Eerten, H., MacFadyen, A., & Zhang, B.-B. 2015, *ApJ*, 799, 3
- Salmonson, J. D. 2003, *ApJ*, 592, 1002
- Sari, R. 1998, *ApJ*, 494, L49
- Sari, R. 1999, *ApJ*, 524, L43
- Sari, R., & Esin, A. A. 2001, *ApJ*, 548, 787
- Sari, R., Piran, T., & Halpern, J. 1999, *ApJ*, 519, L17
- Sari, R., Piran, T., & Narayan, R. 1998, *ApJ*, 497, L17
- Sobacchi, E., Granot, J., Bromberg, O., & Sormani, M. C. 2017, *MNRAS*, 472, 616
- Soderberg, A. M., Frail, D. A., & Wieringa, M. H. 2004, *ApJ*, 607, L13
- Taylor, G. B., & Granot, J. 2006, *Mod. Phys. Lett. A*, 21, 2171
- Taylor, G. B., et al. 2005, *ApJ*, 634, L93
- Totani, T. & Panaiteescu, A. 2002, *ApJ*, 576, 120
- Troja, E., et al. 2017, *Natur*, 551, 71
- van der Horst, A. J., Kamble, A., Resmi, L., et al. 2008, *A&A*, 480, 35
- van Eerten, H. J., & MacFadyen, A. I. 2012, *ApJ*, 751, 155
- van Eerten, H. J., & MacFadyen, A. I. 2012, *ApJ*, 747, L30
- van Eerten, H. J., Zhang, W.-Q., & MacFadyen, A. 2010, *ApJ*, 722, 235
- van Eerten, H. J., Leventis, K., Meliani, Z., Wijers, R. A. M. J., & Keppens, R. 2010, *MNRAS*, 403, 300
- van Eerten, H., van der Horst, A., & MacFadyen, A. 2012, *ApJ*, 749, 44
- van Marle, A. J., Langer, N., Achterberg, A., & García-Segura, G. 2006, *A&A*, 460, 105
- Waxman E., 1997, *ApJ*, 491, L19
- Woods, E., & Loeb, A. 1999, *ApJ*, 523, 187
- Wijers, R. A. M. J., & Galama, T. J. 1999, *ApJ*, 523, 177
- Wygoda N., Waxman E., & Frail D. A., 2011, *ApJ*, 738, L23
- Xu, M., Nagataki, S., & Huang, Y. F. 2011, *ApJ*, 735, 3
- Zhang, B., & Mészáros, P. 2002, *ApJ*, 571, 876
- Zhang W., & MacFadyen A. I., 2009, *ApJ*, 698, 1261
- Zou, Y. C.; Wu, X. F.; Dai, Z. G. 2007, *A&A*, 461, 115

This paper has been typeset from a  $\text{\TeX}/\text{\LaTeX}$  file prepared by the author.